Draft version October 30, 2023
Typeset using LaTeX **twocolumn** style in AASTeX631

Using Bayesian Methods to Interpret LISA Gravitational Wave Observations and Infer Common Envelope Evolution

Ashlin Varghese,[1] Valeriya Korol,[2] Alejandro Vigna-Gómez,[2] Stephan Justham,[2] Carles Badenes,[3] Katelyn Breivik,[4] and Nikolaos Karnesis[5]

[1] *Newcastle University, Newcastle Upon Tyne, NE17RU, UK*
[2] *Max-Planck-Institut für Astrophysik, Karl-Schwarzschild-Straße 1, 85741, Garching, Germany*
[3] *University of Pittsburgh, Pittsburgh, PA, US*
[4] *Carnegie Mellon University, Pittsburgh, PA, US*
[5] *Department of Physics, Aristotle University of Thessaloniki, Thessaloniki 54124, Greece*

ABSTRACT

Galactic double white dwarfs (DWDs) are considered to be a major gravitational wave source detectable by the Laser Interferometer Space Antenna (LISA). It has been shown that they can be used as a tool to study the properties of the Milky Way and nearby galaxies. For this project, we employ a suit of mock DWD catalogues compiled with the binary population synthesis technique. We examine sub-population with the signal to noise ratio > 7, which we consider to be resolvable by LISA as individual GW sources. The remaining sources constitutes the Galactic GW foreground confusion signal. Using Bayesian statistics methods, we aim to constrain the total stellar mass of the Milky way using both: the total number of resolvable DWDs and the amplitude of the Galactic foreground signal. This project is started as part of the Kavli Summer Program 2023.

1. INTRODUCTION

The Laser Interferometer Space Antenna (LISA) is set to be the first European space-borne Gravitational Wave (GW) observatory probing the frequency range from 0.1 to 100 mHz. LISA is expected to map several massive black hole binaries and thousands of galactic binaries consisting of white dwarfs, neutron stars and (stellar-mass) black holes. At low frequencies, galactic binaries are thought to be so numerous that their individual detection are limited by confusion with other binaries yielding a stochastic GW foreground or confusion signal. Along with the galactic binaries and massive black hole binaries, LISA can also provide information about this galactic foreground signal (Amaro-Seoane et al. 2017).

Among the several types of binaries observed, one of the primary targets of LISA are the short orbital period double white dwarfs (DWDs). Short orbital period DWDs (<1 hour) emit gravitational waves that lies within the frequency range of LISA. Tens of thousands of DWDs are expected to be detected by LISA (Amaro-Seoane et al. 2023). Being so numerous, they can be used as a tool to derive the properties of the Milky Way such as the total stellar mass (Georgousi et al. 2022), structure (Korol et al. 2019), and potentially also its star formation history (SFH) and the initial mass function (IMF) (e.g. Tremblay et al. 2014; Kilic et al. 2019, using single white dwarfds). Furthermore, the chirp mass obtained from the orbital- decay rate measured by LISA can be combined with the EM observations to determine the mass of the WD components.

However, the current observed sample of short-period DWDs suffers from selection effects and biases, which makes it challenging to forward model predictions for LISA. Therefore, binary population synthesis is often used in the literature to forecast LISA observations (Nelemans et al. 2001; Ruiter et al. 2010; Yu & Jeffery 2010; Nissanke et al. 2012; Korol et al. 2017; Lamberts et al. 2019; Breivik et al. 2020; Li et al. 2020; van Zeist et al. 2023). When using this technique there are a number of assumptions to be made, but the most impactful one is about the common envelope (CE) phase (e.g. Toonen et al. 2012). It is expected that a typical close orbit DWDs have undergone at least two mass transfer phases, one of which is thought to be unstable, resulting in the formation of a CE (e.g. Nelemans et al. 2004). There are two formalism of CE which are often used in the binary population synthesis codes when studying DWDs. These are the alpha (α) formalism and the gamma (γ) formalism (for a review see Ivanova et al. 2013). The α formalism is a theoretical formalism based on equating the energy balance in the system. However, when this formalism was used to reconstruct observed DWD binaries with accurate mass component mass measurements from spectroscopy, the α formalism

was not successful in reproducing the observed mass ratio distributions, and therefore the gamma formalism was proposed (Nelemans et al. 2000). This alternative formalism is based on the angular momentum balance. In the α formalism. the orbit is always shrinks, wheres it can widen in γ formalism; therefore, typically γ formalism is expected to be the first mass transfer phase in a system.

In this work, we aim to assess LISA's ability to determine the properties of the underlying stellar population of the Milky Way by studying the spectral shape of the Galactic DWD confusion foreground signal (unresolved by LISA), as well as the sample of resolved DWDs individually detectable by LISA. We use a catalogue of DWDs using binary population synthesis model. Starting from Georgousi et al. (2022), we consider their catalogues of resolved sources and the respective foreground. The focus of this study is to assess differences between various models using different CE formalisms. We then find an empirical solution to various foreground signals and determine the properties such as the number of DWDs contributing to them. Than, the total stellar mass of the Galaxy can be derived from the total energy emitted in GWs by the Galactic DWD population. The stellar population synthesis models provide the stellar-mass-light-ratio by combining the stellar isochrones, spectral libraries and the initial star formation history (e.g. Bruzual A. 1983; Nesti & Salucci 2013). The total stellar mass of a galaxy can then be derived by fitting this to a synthetic data or to observations. In analogy with this technique, here we determine the stellar mass of the galaxy combining our knowledge of the number resolved DWDs and the confusion signal and then study the underlying binary evolution model (varying only the CE prescription).

2. METHODOLOGIES

2.1. *Binary population synthesis catalogues*

We utilized a suite of mock DWD catalogues, which were generated using the binary population synthesis code SeBa (Portegies Zwart & Verbunt 1996; Nelemans et al. 2001; Toonen et al. 2012). These catalogues consider a solar metallicity and adopt the Kroupa et al. (1993) initial mass function within the mass range of $0.09 - 10M_{\odot}$. They were created by assuming both α and γ CE formalisms and incorporating various efficiencies (for α and γ parameters) as detailed in Table 1.

The parameter α is the measure of the CE efficiency with the higher values of α corresponding to a more efficient envelope ejection. This is encoded in the SeBa simulation through $\alpha\lambda$ product. Here, the parameter λ represent the envelope's binding energy (see Toonen et al. 2012, for details). In this work we consider models corresponding to variations: $\alpha\lambda = 2$ (referred to as $\alpha\alpha$ in Table 1), which is the fiducial assumption and $\alpha\lambda = 0.25$ (referred to as $\alpha\alpha2$ in Table 1). The γ-CE formalism is applied to our $\gamma\alpha$ models with $\gamma = 1.75$, but considers α-CE with $\alpha\lambda = 2$ when the companion is a degenerate object or when it undergoes a dynamically unstable mass-transfer (Nelemans et al. 2001). Our $\alpha\alpha$ and $\gamma\alpha$ models which has $\alpha\lambda = 2$ are calibrated using the observed DWDs (particularly the second mass-transfer phase, see Nelemans et al. 2000, 2001). On the other hand, the models with $\alpha\lambda = 0.25$ ($\alpha\alpha2$ and $\gamma\alpha2$) are calibrated based on the compact WDs formation in binaries with M type main-sequence stars (Zorotovic et al. 2010; Toonen & Nelemans 2013; Camacho et al. 2014; Zorotovic et al. 2014). We note that recent studies by Scherbak & Fuller (2023) and Kilic et al. (2023) hints that the efficiency obtained from reconstructing the DWDs evolution might be closer to our $\alpha\alpha2$ and $\gamma\alpha2$ models.

As we aim to recover the (underlying) total stellar mass of the Galaxy ($M_{\rm tot}$) based on LISA's observations, the number of resolved sources can be connected to each of our models as follows. We consider the relation between binary mass fraction and the mass of the primary and secondary sources. Given the total number of binary sources simulated from SeBa is 25000, the binary fraction $f_{\rm bin}$, the proportion of the stellar mass interval simulated compared to the total mass interval according to the Kroupa et al. (1993) IMF is 0.096, and the average masses of binary and single stars in our simulations (0.74 M$\odot$ and 0.49 M$\odot$ respectively), we have the total mass corresponding to the simulated population as

$$M_{\rm tot}(f_{\rm bin}) = \frac{250000}{0.096}\left[0.74 f_{\rm bin} + 0.49(1 - f_{\rm bin})\right]. \quad (1)$$

Given this relation as assuming that binary fraction does not correlate with the other assumption (see Thiele et al. 2023, challenging this assumption), it is sufficient to perform a binary population synthesis simulation using one single assumption of $f_{\rm bin}$ as the result can be be re-scaled using Eqn.(1). All of our models have been obtained assuming $f_{\rm bin} = 0.5$. The scaling factor for different values of f_{bin} can be computed as

$$\text{scaling factor} = \frac{M_{\rm tot}(f_{\rm bin})}{M_{\rm tot}(f_{\rm bin} = 0.5)} \quad (2)$$

2.2. *LISA catalogues processing pipeline*

To obtain the number of DWDs ($N_{Lisa,band}$) given in Table 1 and their present-day properties (as binary population synthesis provides binary properties at DWD

CE formalism	$\alpha\lambda$	γ	$N_{\mathbf{LISA,band}}$ $\times 10^6$	$N_{\mathbf{SNR>7}}$ $\times 10^3$
$\alpha\alpha$	2	–	21	24
$\alpha\alpha 2$	0.25	–	0.0235	0.749
$\alpha\gamma$	2	1.75	29	26
$\alpha\gamma 2$	0.25	1.75	14	21

Table 1: The efficiency parameters $\alpha\lambda$ and γ for the different CE formalism's considered and the respective number of binaries in the LISA frequency band ($N_{\mathbf{LISA,band}}$) and those with SNR$>$ 7 ($N_{\mathbf{SNR>7}}$) considered as resolved by LISA.

formation), we re-sample DWDs considering the total mass of the Milky Way and its star formation rate as in Korol et al. (2019). These DWDs are then processed in LISA pipeline (Karnesis et al. 2021) to separate sources with signal-to-noise ratio (SNR) >7 – categorised as the resolvable sources – from the confusion foreground. We utilise results from Georgousi et al. (2022) where GW signals were simulated from the population of N sources, each described by a set of eight parameters $\vec{\theta} = \{f, \dot{f}, \mathcal{A}, \beta, \lambda, \iota, \psi, \phi_0\}$. Here, $\mathcal{A}$ is the strain amplitude, f is the GW emission frequency and $\dot{f}$ is its derivative; ψ and ϕ_0 corresponds to the polarisation and the wave's initial phase respectively; β, λ and ι are the localisation parameters.

The gravitational wave amplitude is measured in terms of the characteristic strain h_c,

$$h_c = \mathcal{A}\sqrt{T_{obs} f_0}, \tag{3}$$

which is proportional to the observing time, T_{obs}. Here $\mathcal{A}$ is the amplitude of the GWs. We then calculated the chirp mass of these resolvable sources using the following equation.

$$\dot{f} = \frac{96}{5}\pi^{\frac{8}{3}}\left(\frac{GM}{c^3}\right)^{\frac{5}{3}} f^{\frac{11}{3}}, \tag{4}$$

where $M = (m_1 m_2)^{\frac{3}{5}}/(m_1 + m_2)^{\frac{1}{5}}$.

As the first step of the LISA catalogue processing pipeline, SNRs of all sources with respect to the instrumental noise is determined without considering any possible overlapping signals (ρ_{opt}). The smoothed power spectral density (PSD) is then computed on these simulated data to make the first estimate of the overall confusion signal S_k by running a median on the PSD of the data followed by fitting a polynomial model or applying Gaussian kernel. Next, SNRs of each source i in the catalogue (ρ_i) is calculated with respect to the obtained S_k. The sources are considered resolvable, if $\rho_i > \rho_{\rm thres}$, where $\rho_{\rm thres} = 7$ is a fixed threshold, and are subtracted from the data. The confusion signal S_{k+1} is estimated after the first iteration and this process iterates until there are no sources to subtract. At the end of the above process, the computation of Fisher Information Matrices (FIMs) is carried out on the resolvable sources with respect to the final $S_{\rm final}$.

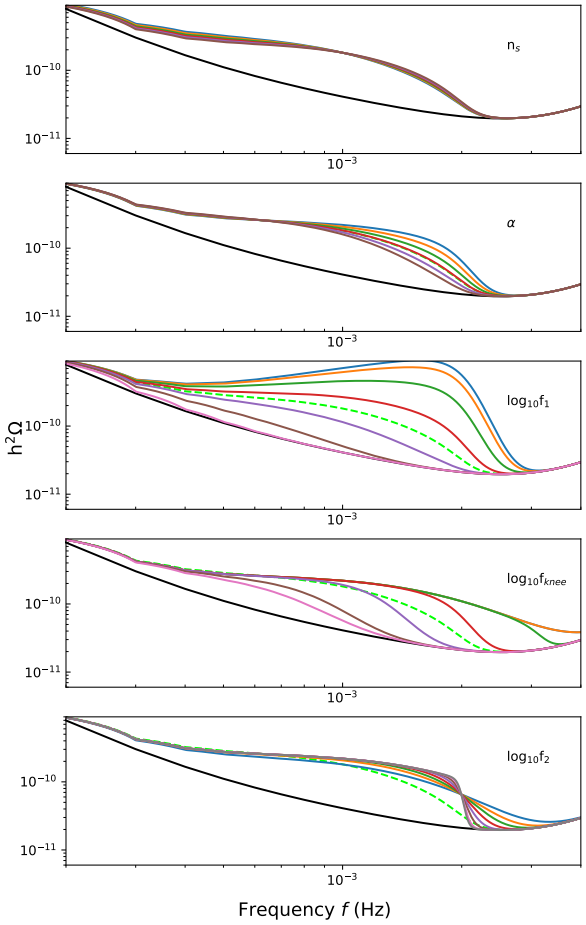

Figure 1: The green dashed line corresponds to Eqn. 7 with $n_{\rm s} = 1.27$, $\alpha = 1.31$, $\log_{10} f_1 = -3.2$, $\log_{10} f_{\rm knee} = -2.7$, and $\log_{10} f_2 = -3.5$. The black solid line represents the instrumental noise. The colored lines represents the variation of the Eqn. 7 as each parameter $\vec{\theta} = \{n_{\rm s}, \log_{10} f_1, \log_{10} f_{\rm knee}, \log_{10} f_2\}$ is varied from $0.8 \times \vec{\theta}_{*,i}$ to $1.2 \times \vec{\theta}_{*,i}$ considering $\alpha\alpha$ model.

The obtained shape of the foreground signal is well-described by an analytic model of the single-sided spectral density $S(f)$ of the gravitational wave strain (Geor-

gousi et al. 2022; Karnesis et al. 2021):

$$S_{\rm gal}(f) = \frac{A}{2} f^{-n_s^S} e^{-(\frac{f}{f_1})^\alpha} 1 + \tanh[(f_{\rm knee} - f)/f_2], \quad (5)$$

where A is the amplitude of the foreground signal, n_s^S is the spectral tilt at low-frequency, the exponential term that includes the parameter f_1 and α gives the loss of stochasticity due to smaller density of sources at higher frequencies and the tanh having the parameters, f_2 and $f_{\rm knee}$ represents the cut off of the signal due to individual removal of bright sources. The expression in Eq.(5) is often used in the LISA mission related literature and therefore we also employ it this study to describe the obtained Galactic foreground from the considered binary population synthesis models.

The spectral density above is related to the energy density of the gravitational waves ρ_{gw} and $\rho_c = 3c^2H_0^2/8\pi G$ through $\Omega = \rho_{gw}/\rho_c$, with

$$h^2\Omega = \frac{4\pi^2 f^3}{3(H_0/h)^2} S(f), \quad (6)$$

where h is the normalised Hubble expansion rate and H_0 is the present value of the Hubble expansion rate. We perform the analysis using Ω as it is customary in the context of the foregrounds/backgrounds studies. For analysis the above equations are combined to get

$$h^2\Omega = 10^{\log_{10}(h^2\Omega^*)} \left(\frac{f}{f_*}\right)^{n_{\rm s}} e^{-(f/10^{\log_{10} f_1})^\alpha} \times \left(1 + \tanh\left[(10^{\log_{10} f_{knee}} - f)/10^{\log_{10} f_2}\right]\right) \quad (7)$$

Here f_* is a fiducial pivot set to 10^{-3}Hz. Fig. 1 shows how $h^2\Omega$ varies as a function of frequency with respect to each of the parameters mentioned above. For illustrative proposes, we used the parameters, $n_{\rm s} = 1.27$, $\alpha = 1.31$, $\log_{10} f_1 = -3.2$, $\log_{10} f_{\rm knee} = -2.7$, and $\log_{10} f_2 = -3.5$ obtained from Georgousi et al. (2022).

3. RESULTS AND DISCUSSIONS

So far there are studies considering just the resolved sources (Korol et al. 2021) and just the foreground sources (Georgousi et al. 2022). In particular, Georgousi et al. (2022) associated the parameters of the residual foreground signal to the total number of sources in the catalogue using the Eqn. 7. In this work, we capitalise on the results of these previous studies to use both the resolved and foreground sources to infer the underlying properties of the Milky Way.

3.1. *Unresolved DWD foreground*

We recall that the Galactic foreground arises from unresolved DWDs which overlap in time and frequencies. Fig. 2 illustrates the comparison between obtained foregrounds with the LISA catalogue processing pipeline (cf. Section 2.2). We show the foregrounds in terms of both characteristic strain (left panel) and energy density (right panel). We see that the characteristic strain and the energy density decreases with increasing frequency, and peaks around, $\sim 1 \times 10^{-3}$Hz. We also note that the $\alpha\alpha2$ model produces no confusion signal.

Next, we now fit Eqn. 7 to the curves in Fig. 2 using the Bayesian fitting through MCMC sampling, for the parameters $\Theta = \{h^2\Omega,\ n_s,\ \alpha,\ f_1,\ f_{knee},\ f_2\}$, for a given model, D,

$$p(\Theta, D) \propto p(\Theta) p(D|\Theta) \quad (8)$$

Here, $p(\Theta)$ are the priors, which are chosen to be uniform for all the parameters mentioned above, and $p(D|\Theta)$ is the likelihood function given by Eqn. 5. We sample posterior distributions, $p(\Theta, D)$, using the affine invariant Markov Chain Monte Carlo (MCMC) ensemble sampler `emcee` (Foreman-Mackey et al. 2013). Table. 2 summarises the obtained parameters with respective 1σ uncertainties, and Fig. 3 shows the posterior distributions for the different models.

We can utilise the information in Fig. 3 to distinguish the different DWD population models studied. We note that, the posterior distributions of $n_{\rm s}$ overlap for all the models making it a less eligible parameter to distinguish between the different formalism. On the other hand, we find posteriors for $f_{\rm knee}$ and f_2 well separated; therefore, these parameters can be used to distinguish the different models. Note again than the model, $\alpha\alpha2$ is not included in Fig. 3, since this model has no foreground (see Fig. 2) and therefore returns flat values as we show in Fig. A.1.

3.2. *Resolved DWDs*

We find that 1 out of 859 sources in $\alpha\alpha$, out of 31 sources in $\alpha\alpha2$, out of 1119 sources in $\gamma\alpha$ and out of 684 sources in $\gamma\alpha2$ are detected in the LISA band. Fig. 4 and Fig. 5 show the characteristic strain as a function of frequencies along with the density and the chirp mass distribution of the resolved sources respectively along with the foreground (black line), for each model. The difference seen between the resolved sources and the foreground in Fig. 5 (i.e. white space between black lines and coloured points) is a consequence of the S/N being set to 7 and the mission duration time set to 4 yr when running the pipeline. We also note that there are more low mass DWDs (black and purple colours) populating high frequencies while high mass DWD (magenta and yellow colours) tend to be more common at lower frequencies. This is because the high mass sources evolve quickly and therefore disappear from high frequencies before the present day. Along with this, the low sen-

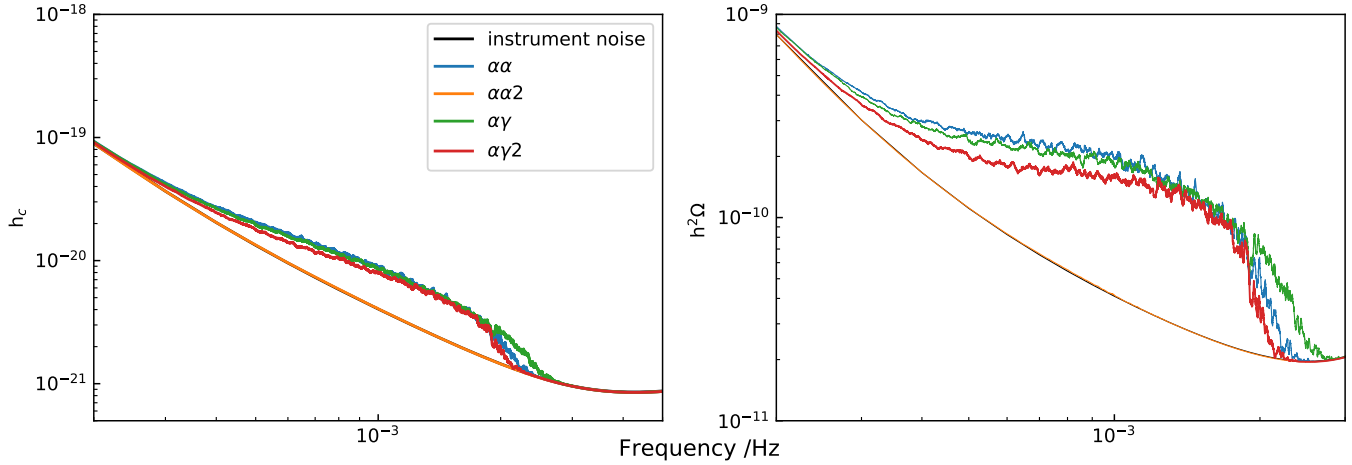

Figure 2: Foreground spectra of all the formalism along with LISA instrumental noise in terms of characteristic strain (h_c) (left) and $h^2\Omega$ (right).

Model	$h^2\Omega$	n_s	α	f_1	f_{knee}	f_2
$\alpha\alpha$	$-9.679^{+0.046}_{-0.049}$	$0.983^{+0.070}_{-0.076}$	$1.545^{+0.093}_{-0.086}$	$-2.996^{+0.031}_{-0.030}$	$\left(-2686.7^{+1.4}_{-1.3}\right)\times10^{-3}$	$\left(-3657.0^{+8.3}_{-9.1}\right)\times10^{-3}$
$\alpha\gamma$	$-9.764^{+0.034}_{-0.032}$	$0.975^{+0.061}_{-0.052}$	$1.597^{+0.066}_{-0.061}$	$-2.962^{+0.021}_{-0.022}$	$\left(-2621.3^{+1.1}_{-1.2}\right)\times10^{-3}$	$-3.634^{+0.011}_{-0.012}$
$\alpha\gamma2$	$-10.012^{+0.036}_{-0.032}$	$0.941^{+0.076}_{-0.060}$	$2.00^{+0.15}_{-0.14}$	$-2.858^{+0.020}_{-0.024}$	$\left(-27145.3^{+10.8}_{-9.9}\right)\times10^{-4}$	$\left(-3790.2^{+6.7}_{-8.7}\right)\times10^{-3}$

Table 2: Parameters for different models

sitivity of low mass sources ones to low frequency also contribute to more low mass sources being distributed at high frequencies. Fig. 6 shows the uncertainty in this mass distribution corresponding to the different models studied in this work.

3.3. *Inferring the underlying stellar mass of the Galaxy*

Given that we have the number of resolved sources and the respective unresolved confusion foreground, we utilize this knowledge to derive the total stellar mass of the Galaxy from the total GWs energy emitted by the DWD population. We also consider the number of binaries per solar mass in the models to get a better constraint of the total stellar mass recovered. This will be discussed in detail in the following sections.

3.3.1. *Estimate based on resolved sources*

To estimate the stellar mass ($M_\star$) of the Milky Way galaxy, given the total number of resolved sources, N, we use the Bayes' theorem, where the posterior on the mass is given as,

$$p(M_\star, N) \propto L(N/M_\star)\pi(M_\star). \tag{9}$$

π ($M_\star$) is the prior and $L(N/M_\star)$ is the likelihood which is assumed to follow a Poisson distribution that can be written as

$$L(N|M_\star) = \textbf{Poisson}(N : \lambda[M_\star] = \frac{\lambda^N exp(-\lambda)}{N!} \tag{10}$$

Here, λ is the expected number of sources given as λ=$M_\star\mu$, where μ is the number of detection per unit solar mass. We also choose a uniform prior within the range $10^9 - 10^{12}$ $M_\odot$. Fig. 7 shows the mass distribution of the galaxy from each model. The total mass of the galaxy ($M_\star$) recovered from the number of resolved sources is given in Table. 3 along with the uncertainties. We note that uncertainties are very small, which is not realistic because these are the statistical uncertainties. To get the systematic uncertainty we utilise our knowledge of number of binary per solar mass in model.

We therefore use the Eqns. 1-2, to determine the scaling factor. We then use this scaling factor to determine the total mass to show the dependence of the binary mass fraction to the total mass. We again use MCMC to constrain the mass parameter and binary mass function by following the same procedure described in section. 3.3.1. For this estimation, Eqn. 9 can be written as,

$$p(M_\star, f_{bin}, N) \propto L(N/M_\star, f_{bin})\pi(M_\star, f_{bin}). \tag{11}$$

π ($M_\star$, f_{bin}) is the prior and $L(N/M_\star, f_{bin})$ is the likelihood. We considered the total mass to be 8×10^{10} $M_\odot$

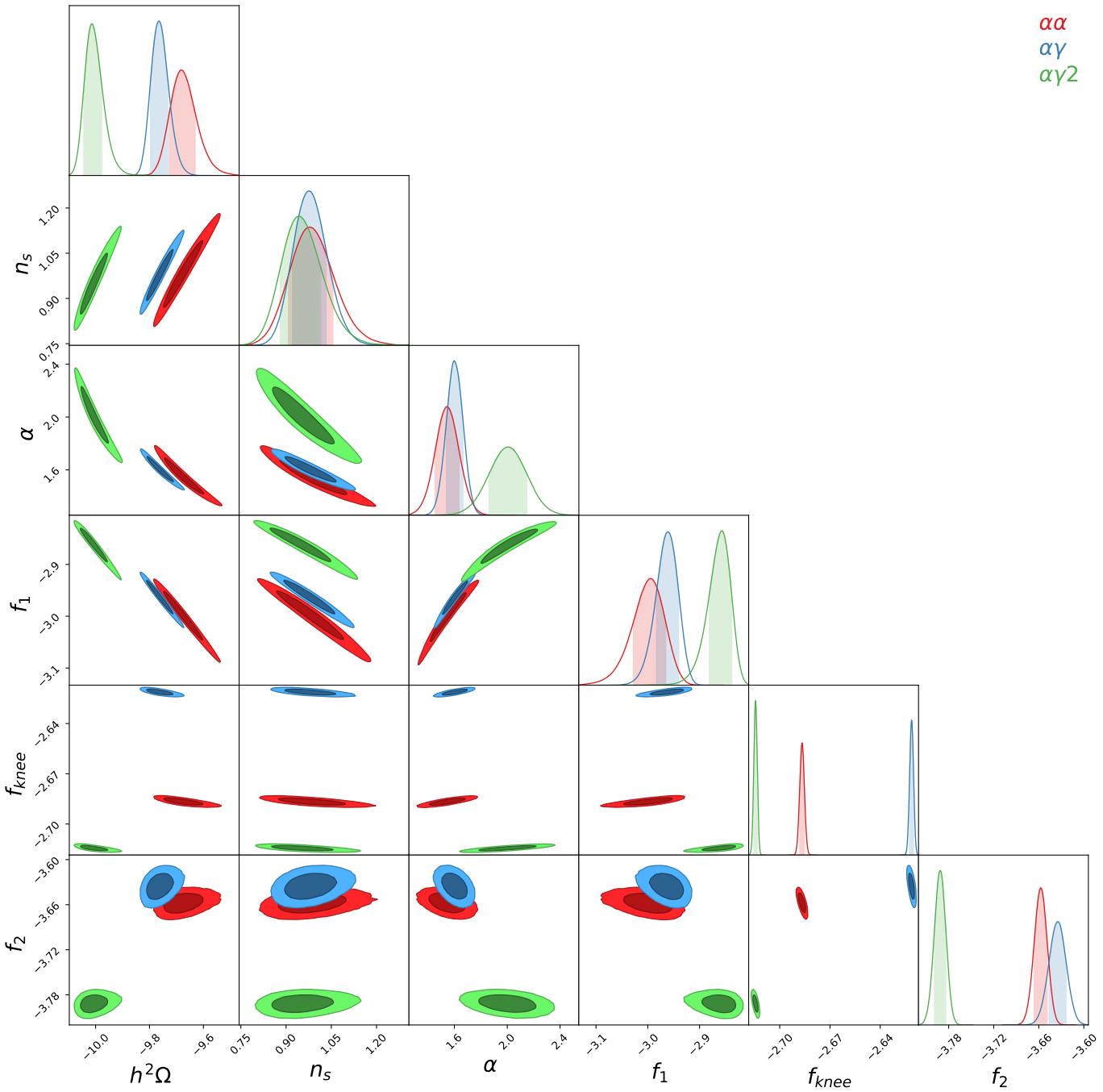

Figure 3: Dependence's of the different parameters, n_s,α, f_1,f_{knee},f_2 for each CE prescription

within the limit 1×10^{10} to 1×10^{12} $M_\odot$ and the binary mass fraction to be in the limit of $0.1 - 0.9$. Table. 3 gives the mass determined ($M_{\star - f_{bin}}$) and Fig. 8 (left) shows the dependence of mass distribution on binary mass fraction for different models along with the uncertainties. We have considered a Gaussian prior for the binary fraction and we see that the error is higher compared to before and therefore it is better constrained. We justify the use of this Gaussian prior from the observations (Offner et al. 2023).

3.3.2. *Estimate based on unresolved foreground*

The next step is to combine the information from foreground and resolved sources. As a first step to combine the information we have from resolved and foreground, we use the inference from foreground to recover the mass as a function of amplitude shown in Fig. 8 (right). We see that the total mass is less than 8×10^{10} $M_\odot$, which is the mass from the foreground only.

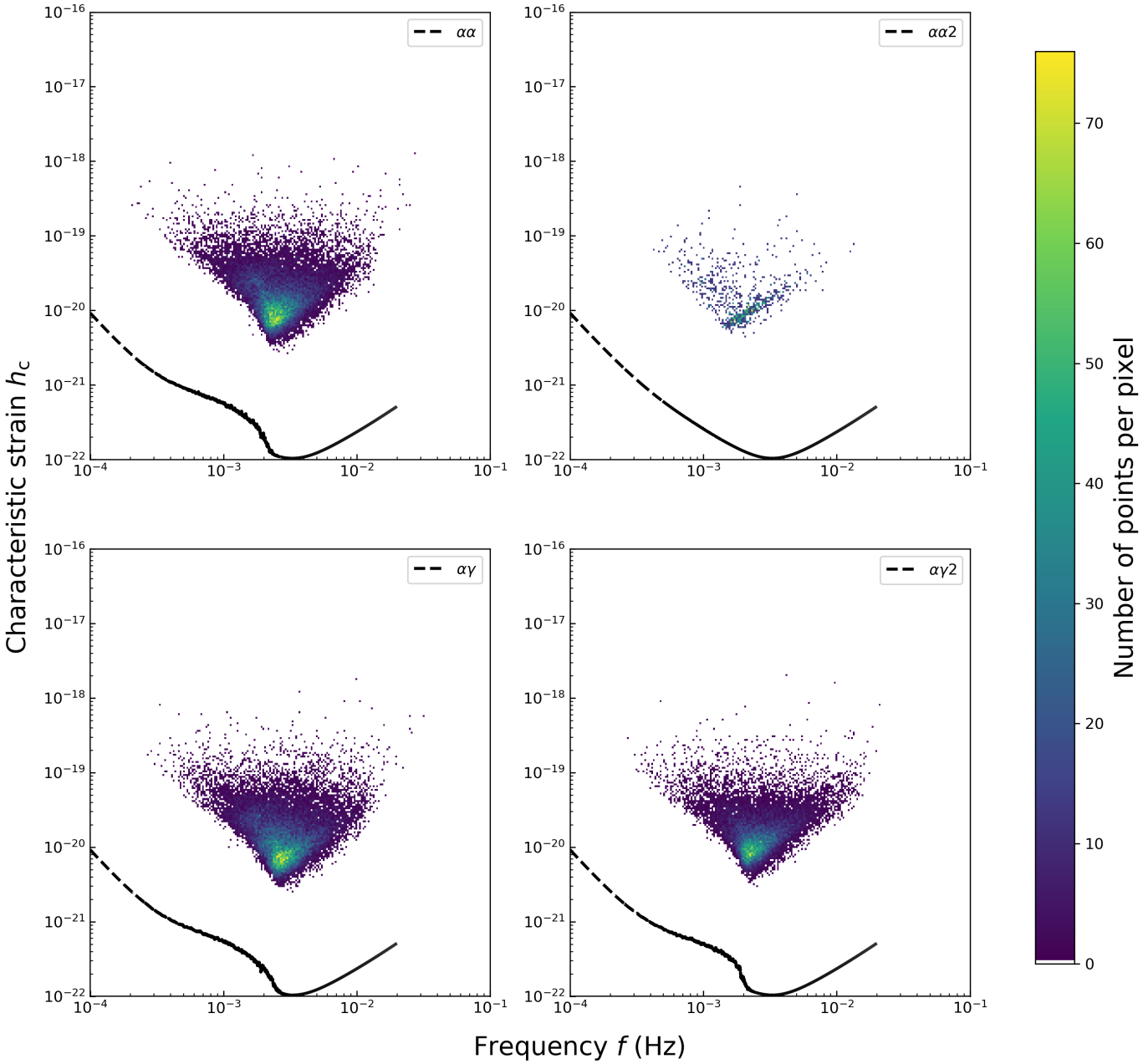

Figure 4: Distribution of detectable sources in terms of characteristic strain, frequency and number density. The black line corresponds to the characteristic strain of the foreground sources.

Fig. 9 shows a comparison of the mass we recovered from resolved and foreground for all models. Based on the fact that the posteriors from the foreground are broader that those from resolved binaries (for respective models), we can conclude that using resolved sources may be sufficient for studying the underlying mass distribution of the Milky Way.

4. CONCLUSIONS

We find that using the foreground sources we were able to distinguish between the different CE formalism. We could also recover the total mass of the galaxy from the resolved sources. We therefore can use the constraint on resolved binaries to predict the amplitude of Galactic unresolved foreground. LISA is sensitive to a number of cosmological scholastic backgrounds that will be superposed in the LISA data together with our Galactic foreground. Our result show that information from resolved binaries will help to disentangle these backgrounds.

Future work will look in to combining the resolved and foreground and also to implement chirp mass distribution to constrain mass from the resolved sources to

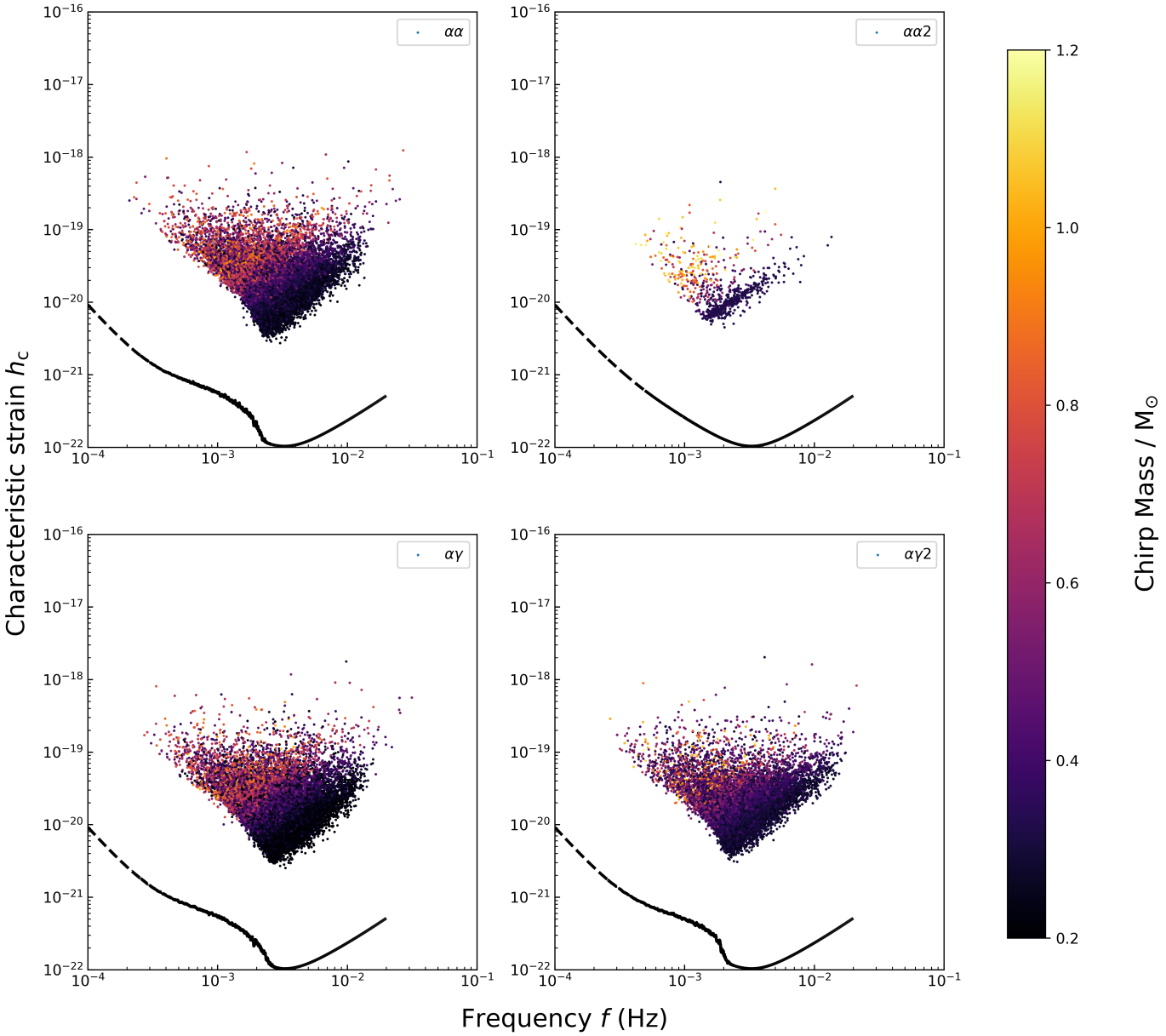

Figure 5: Distribution of detectable sources in terms of characteristic strain, frequency and chirp mass

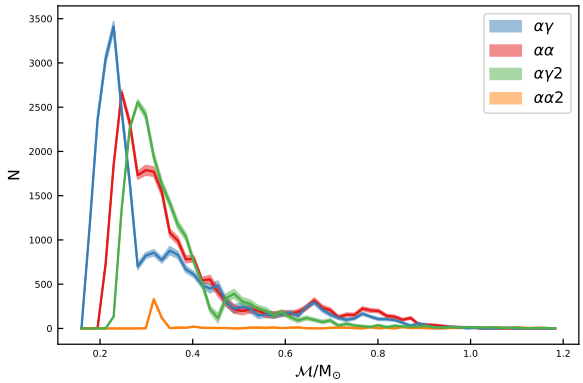

Figure 6: Foreground spectra of all the formalism along with LISA instrumental noise.

Model	$M_\star$	f_{bin}	$M_{\star - f_{bin}}$
$\alpha\alpha$	$(820.3^{+5.0}_{-5.6}) \times 10^8$	$0.50^{+0.20}_{-0.22}$	$(80.9^{+7.7}_{-6.1}) \times 10^9$
$\alpha\alpha 2$	$(81.8^{+3.3}_{-2.7}) \times 10^9$	$0.47^{+0.22}_{-0.19}$	$(81.7^{+7.6}_{-7.2}) \times 10^9$
$\alpha\gamma$	$(819.5^{+5.7}_{-4.6}) \times 10^8$	$0.47^{+0.22}_{-0.19}$	$(81.2^{+7.3}_{-6.3}) \times 10^9$
$\alpha\gamma 2$	$(819.6^{+6.1}_{-5.4}) \times 10^8$	$0.48^{+0.21}_{-0.20}$	$(81.1^{+7.4}_{-6.3}) \times 10^9$
Prior(f_{bin})	–	$0.48^{+0.22}_{-0.18}$	–

Table 3: $M_\star$ represent the total stellar mass of the galaxy recovered from the resolved sources. f_{bin} is the binary mass fraction and $M_{\star - f_{bin}}$ is the mass recovered when the binary mass fraction is included.

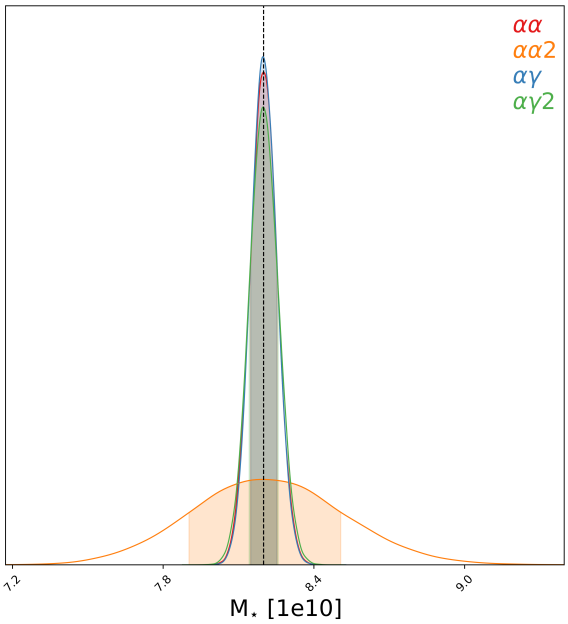

Figure 7: Total stellar mass of the galaxy recovered from the resolved sources

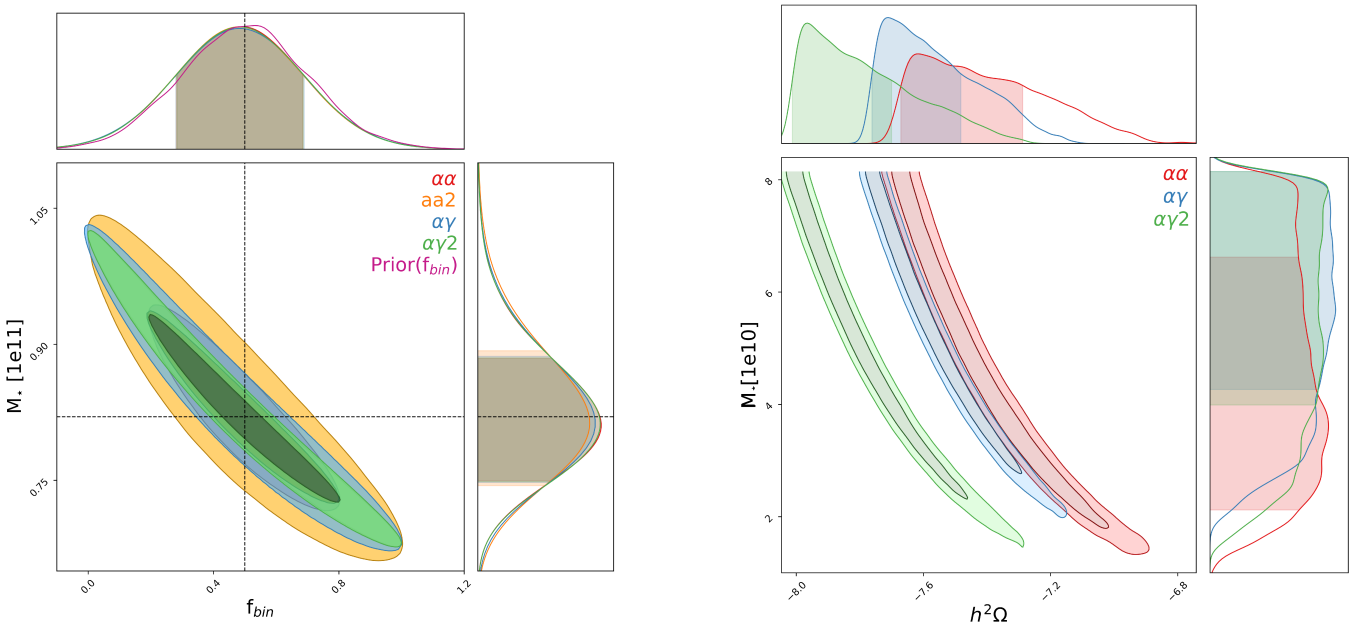

Figure 8: (left) Total stellar mass distribution of the galaxy for the different models considering the total number of resolved binaries and the binary mass fraction (f_{bin}). (right) Mass recovered from the foreground.

better discriminate between CE models. We will then expand the framework to include more models.

5. ACKNOWLEDGMENTS

The authors acknowledge the support of Kavli Foundation and The Max Planck Institute of Astrophysics for the opportunity to conduct this research study.

APPENDIX

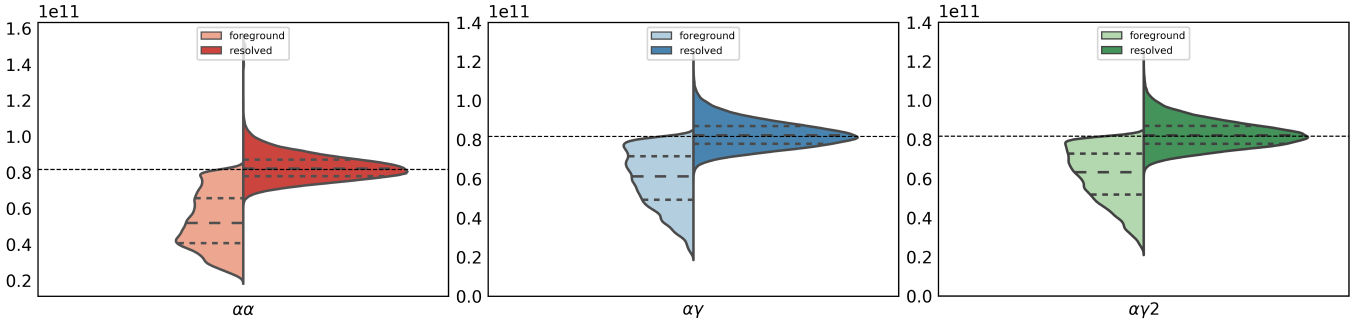

Figure 9: Mass recovered from resolved and foreground for (red) $\alpha\alpha$, (blue) $\alpha\gamma$, and (green) $\alpha\gamma2$ models.

A. APPENDIX INFORMATION

The summary Fig. A.1 showing all the parameters corresponding to Fig. 3. We see that $\alpha\alpha2$ model returns a flat value indicating that it has no foreground.

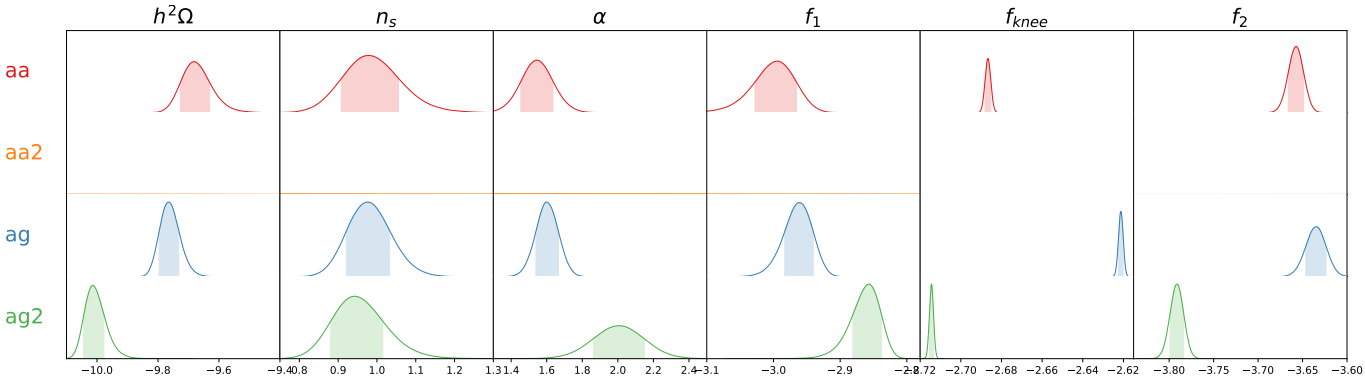

Figure A.1: Summary distribution of the different parameters, n_s, α, f_1, f_{knee}, f_2 for each CE prescription.

REFERENCES

Amaro-Seoane, P., Audley, H., Babak, S., et al. 2017, arXiv e-prints, arXiv:1702.00786, doi: 10.48550/arXiv.1702.00786

Amaro-Seoane, P., Andrews, J., Arca Sedda, M., et al. 2023, Living Reviews in Relativity, 26, 2, doi: 10.1007/s41114-022-00041-y

Breivik, K., Mingarelli, C. M. F., & Larson, S. L. 2020, ApJ, 901, 4, doi: 10.3847/1538-4357/abab99

Bruzual A., G. 1983, ApJ, 273, 105, doi: 10.1086/161352

Camacho, J., Torres, S., García-Berro, E., et al. 2014, A&A, 566, A86, doi: 10.1051/0004-6361/201323052

Foreman-Mackey, D., Hogg, D. W., Lang, D., & Goodman, J. 2013, PASP, 125, 306, doi: 10.1086/670067

Georgousi, M., Karnesis, N., Korol, V., Pieroni, M., & Stergioulas, N. 2022, Monthly Notices of the Royal Astronomical Society, 519, 2552, doi: 10.1093/mnras/stac3686

Ivanova, N., Justham, S., Chen, X., et al. 2013, A&A Rv, 21, 59, doi: 10.1007/s00159-013-0059-2

Karnesis, N., Babak, S., Pieroni, M., Cornish, N., & Littenberg, T. 2021, Phys. Rev. D, 104, 043019, doi: 10.1103/PhysRevD.104.043019

Kilic, M., Bergeron, P., Dame, K., et al. 2019, MNRAS, 482, 965, doi: 10.1093/mnras/sty2755

Kilic, M., Moss, A. G., Kosakowski, A., et al. 2023, MNRAS, 518, 2341, doi: 10.1093/mnras/stac3182

Korol, V., Belokurov, V., Moore, C. J., & Toonen, S. 2021, MNRAS, 502, L55, doi: 10.1093/mnrasl/slab003

Korol, V., Rossi, E. M., & Barausse, E. 2019, MNRAS, 483, 5518, doi: 10.1093/mnras/sty3440

Korol, V., Rossi, E. M., Groot, P. J., et al. 2017, MNRAS, 470, 1894, doi: 10.1093/mnras/stx1285

Kroupa, P., Tout, C. A., & Gilmore, G. 1993, MNRAS, 262, 545, doi: 10.1093/mnras/262.3.545

Lamberts, A., Blunt, S., Littenberg, T. B., et al. 2019, MNRAS, 490, 5888, doi: 10.1093/mnras/stz2834

Li, Z., Chen, X., Chen, H.-L., et al. 2020, ApJ, 893, 2, doi: 10.3847/1538-4357/ab7dc2

Nelemans, G., Verbunt, F., Yungelson, L. R., & Portegies Zwart, S. F. 2000, A&A, 360, 1011. https://arxiv.org/abs/astro-ph/0006216

Nelemans, G., Yungelson, L. R., & Portegies Zwart, S. F. 2001, A&A, 375, 890, doi: 10.1051/0004-6361:20010683

Nelemans, G., Yungelson, L. R., & Portegies Zwart, S. F. 2004, Monthly Notices of the Royal Astronomical Society, 349, 181, doi: 10.1111/j.1365-2966.2004.07479.x

Nesti, F., & Salucci, P. 2013, Journal of Cosmology and Astroparticle Physics, 2013, 016, doi: 10.1088/1475-7516/2013/07/016

Nissanke, S., Vallisneri, M., Nelemans, G., & Prince, T. A. 2012, ApJ, 758, 131, doi: 10.1088/0004-637X/758/2/131

Offner, S. S. R., Moe, M., Kratter, K. M., et al. 2023, in Astronomical Society of the Pacific Conference Series, Vol. 534, Protostars and Planets VII, ed. S. Inutsuka, Y. Aikawa, T. Muto, K. Tomida, & M. Tamura, 275, doi: 10.48550/arXiv.2203.10066

Portegies Zwart, S. F., & Verbunt, F. 1996, A&A, 309, 179

Ruiter, A. J., Belczynski, K., Benacquista, M., Larson, S. L., & Williams, G. 2010, ApJ, 717, 1006, doi: 10.1088/0004-637X/717/2/1006

Scherbak, P., & Fuller, J. 2023, MNRAS, 518, 3966, doi: 10.1093/mnras/stac3313

Thiele, S., Breivik, K., Sanderson, R. E., & Luger, R. 2023, ApJ, 945, 162, doi: 10.3847/1538-4357/aca7be

Toonen, S., & Nelemans, G. 2013, A&A, 557, A87, doi: 10.1051/0004-6361/201321753

Toonen, S., Nelemans, G., & Portegies Zwart, S. 2012, A&A, 546, A70, doi: 10.1051/0004-6361/201218966

Tremblay, P. E., Kalirai, J. S., Soderblom, D. R., Cignoni, M., & Cummings, J. 2014, ApJ, 791, 92, doi: 10.1088/0004-637X/791/2/92

van Zeist, W. G. J., Eldridge, J. J., & Tang, P. N. 2023, MNRAS, 524, 2836, doi: 10.1093/mnras/stad1976

Yu, S., & Jeffery, C. S. 2010, A&A, 521, A85, doi: 10.1051/0004-6361/201014827

Zorotovic, M., Schreiber, M. R., Gänsicke, B. T., & Nebot Gómez-Morán, A. 2010, A&A, 520, A86, doi: 10.1051/0004-6361/200913658

Zorotovic, M., Schreiber, M. R., García-Berro, E., et al. 2014, A&A, 568, A68, doi: 10.1051/0004-6361/201323039